

Article

# Thermal Deactivation of Rh/ $\alpha$ -Al<sub>2</sub>O<sub>3</sub> in the Catalytic Partial Oxidation of Iso-Octane: Effect of Flow Rate

Roberto Batista , Andrea Carrera , Alessandra Beretta \*  and Gianpiero Groppi \*

Laboratory of Catalysis and Catalytic Processes, Dipartimento di Energia, Politecnico di Milano, via La Masa 34, 20156 Milano, Italy; roberto.batistadasilva@polimi.it (R.B.); andrea.carrera@polimi.it (A.C.)

\* Correspondence: alessandra.beretta@polimi.it (A.B.); gianpiero.groppi@polimi.it (G.G.);  
Tel.: +39-02-23993284 (A.B.); +39-02-23993264 (G.G.)

Received: 20 May 2019; Accepted: 12 June 2019; Published: 14 June 2019



**Abstract:** Catalytic partial oxidation (CPO) of logistic fuels is a promising technology for the small-scale and on-board production of syngas (H<sub>2</sub> and CO). Rh coated monoliths can be used as catalysts that, due to Rh high activity, allow the use of reduced reactor volumes (with contact time in the order of milliseconds) and the achievement of high syngas yield. As the CPO process is globally exothermic, it can be operated in adiabatic reactors. The reaction mechanism of the CPO process involves the superposition of exothermic and endothermic reactions at the catalyst inlet. Thus, a hot spot temperature is formed, which may lead to catalyst deactivation via sintering. In this work, the effect of the flow rate on the overall performance of a CPO-reformer has been studied, using iso-octane as model fuel. The focus has been on thermal behavior. The experimental investigation consisted of iC8-CPO tests at varying total flow rates from 5 to 15 NL/min, wherein axially resolved temperature and composition measurements were performed. The increase of flow rate resulted in a progressive increase of the hot spot temperature, with partial loss of activity in the entry zone of the monolith (as evidenced by repeated reference tests of CH<sub>4</sub>-CPO); conversely, the adiabatic character of the reformer improved. A detailed modelling analysis provided the means for the interpretation of the observed results. The temperature hot spot can be limited by acting on the operating conditions of the process. However, a tradeoff is required between the stability of the catalyst and the achievement of high performances (syngas yield, reactants conversion, and reactor adiabaticity).

**Keywords:** CPO reactor; effect of flow rate; deactivation; iso-octane; Rh catalysts

## 1. Introduction

Nowadays, the industrial sector (mining, manufacturing, agriculture, construction, and others) accounts for the largest share in energy consumption all around the world. According to IEA, the transportation sector ranks at the second position in terms of energy consumption and projections show that, in the 2015–2040 period, its demand for energy will grow more quickly than the industrial field, reaching 1%/year, 0.3% higher than the industrial rate [1]. To supply this ever-increasing demand, while coping with the commitment to mitigating CO<sub>2</sub> emissions, fuel cell and hydrogen technology can be a key player [2,3]. The final goal of a green energy market is the full exploitation of renewable energy sources (with H<sub>2</sub> production via water electrolysis); however, the development of a decentralized H<sub>2</sub>-production and supply chain based on small scale processors represents a realistic transition strategy [4–7]. Small-scale reformers have also been proposed for the on-board applications of H<sub>2</sub> (fueling of auxiliary power units based on fuel cells, the injections in the combustion chamber, and the regeneration of catalytic traps) in view of an improvement of the vehicle efficiency [8–11].

Natural gas, LPG, and liquid hydrocarbons can be converted catalytically into hydrogen-rich steams by steam reforming (SR) and catalytic partial oxidation (CPO). The use of noble metal-based

catalysts is an important aspect of the process intensification, since higher activity allows for smaller catalyst inventory and faster dynamic response. Furthermore, such catalysts reduce the risk of coke formation with respect to non-precious metals as Ni and Fe [12,13]. Operating at very short contact times mitigates the cost issues associated with the adoption of precious metal catalysts. Among noble metals, Rh was reported to provide the highest activity and lower the tendency to coke formation at typical CPO conditions [4,14,15].

Concerning the reactor design, steam reforming of methane is an already consolidated industrial technology based on multi-tubular reactors but the necessity of a large energy input due to its high endothermicity makes the reactors hardly scalable down to small sizes (1–10 kW) of interest for distributed applications [2,16–19]. Instead, the catalytic partial oxidation (CPO) of hydrocarbons is a more flexible technology as it is globally exothermic and can be carried out in simple adiabatic structured reactors that are easily scalable.

The autothermal operation of the so-called short contact time CPO reformers has been successfully demonstrated by the pioneering and extensive work of Lanny Schmidt and coworkers, who have shown the obtainment of high syngas yields via partial oxidation of gaseous and vaporized liquid hydrocarbons over Rh washcoated foams [20–23]. The results from the Minnesota group have been largely confirmed in the years by several groups [24–27]. Besides, the development of advanced experimental and modelling tools has significantly contributed to the comprehension of the transport and chemical phenomena that govern the performance of CPO reformers [28]. Basini and co-workers have addressed a comprehensive analysis of the reduction of investment costs and energy consumption, the flexibility towards feedstock composition and product capacity, and the simplicity of technical and operational processes [29].

In previous works, the authors have reported the results of recent studies on the autothermal CPO of model hydrocarbons, representative of logistic fuels: iso-octane (iC8), a model for gasoline; and n-octane, a model for diesel [19,30]. The measurement of axially resolved temperature and concentration profiles and the engineering analysis of the reactor by the means of mathematical modelling have shown that the CPO of logistic fuels is a more severe process than the CPO of light hydrocarbons, being characterized by a higher peak surface temperature and the onset of gas-phase reactions leading to the formation of coke precursors; both factors can significantly contribute to accelerate catalyst deactivation by sintering and coking [17,19,30].

In this work, the effect of the input load on the performance of an iC8-CPO reformer was investigated by both experimental and modelling approaches. Flow rate is a key parameter of the reformer performance; it affects the reaction pathways, the output product yield, and the extent of heat dissipations. In turn, these factors can significantly impact the thermal behavior of the reactor and, consequently, the catalyst stability. At this scope, experiments and calculations were performed for a 400/7 CPSI cordierite honeycomb monolith, coated with a 2 wt% Rh/  $\alpha$ -Al<sub>2</sub>O<sub>3</sub> active phase.

## 2. Results and Discussion

### 2.1. Conversion and Selectivity Performances

Experiments of iC8-CPO were performed at constant feed composition (iC8, Air, N<sub>2</sub> with 3% iC8 and C/O = 0.9) and varying total flow rate from 5 to 15 NL/min; Figure 1 reports the integral results of the experiments in terms of reactant conversions and product yields.

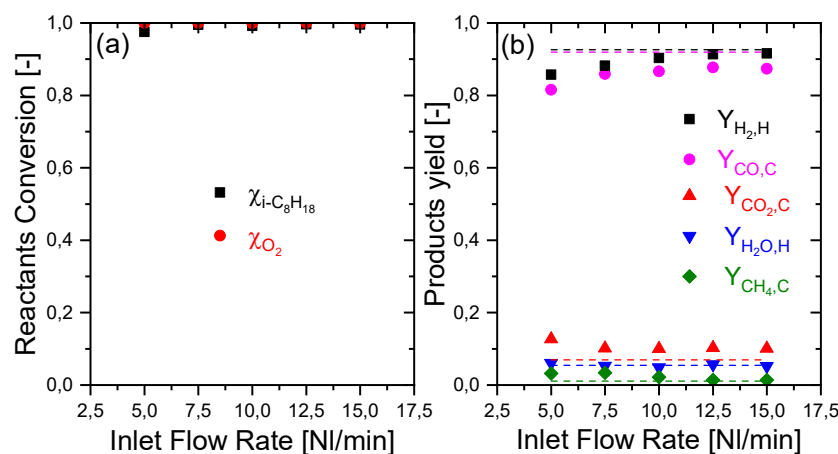


**Figure 1.** Effect of flow rate on the integral performance of the catalytic partial oxidation (CPO) reactor: (a) reactants conversion ( $\chi$ ); (b) products yield ( $Y_{i,j}$ ,  $i = \text{product}$  and  $j = \text{reference atom balance}$ ). Feed composition: iC8 = 3%, air with C/O = 0.9 and N<sub>2</sub> complement. Symbols = experiments; dashed lines = calculated adiabatic equilibrium.

It was verified that O<sub>2</sub>, the limiting reactant, was fully converted under all the conditions. Except in the case of 5 NL/min, iso-octane was also completely converted since its conversion was not limited by thermodynamics. At increasing flow rate, the selectivity and yield of H<sub>2</sub> and CO increased, progressively approaching the expected equilibrium values under adiabatic conditions (dotted lines in Figure 1). The yields of CH<sub>4</sub>, CO<sub>2</sub>, and H<sub>2</sub>O, instead, moderately decreased and tended to the calculated equilibrium values as inlet flow increased. This result might appear counter-intuitive, considering the indirect-consecutive nature of CO and H<sub>2</sub> formation and the expected negative effect of reducing the contact time on the formation of terminal products. However, the axial evolution of temperature profiles changed considerably at increasing flow rates; the measurements obtained during the iso-octane experimental campaign are presented in Figure 2, where thin lines represent the measurements obtained by the thermocouple (representative of the gas-phase temperature), while thicker lines represent the measurements obtained from the optical-fiber/pyrometer system (representative of the emitting surface temperature).

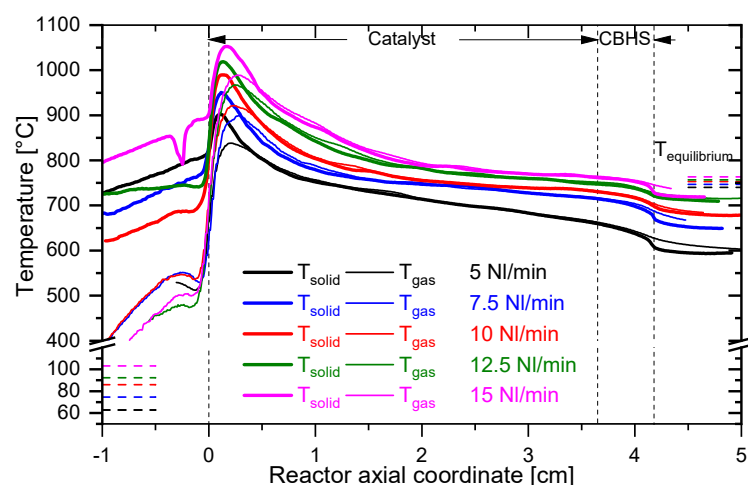


**Figure 2.** Experimental temperature profiles varying the inlet flow rate. Feed composition: iC8 = 3%, Air with C/O = 0.9 and N<sub>2</sub> complement ( $T_{\text{solid}}$  measured with an optical fiber and  $T_{\text{gas}}$  measured with a thermocouple).

The temperature of the catalyst surface and of the gas phase measured along the entire axial coordinate increased significantly with the increase of flow rate. Several factors have a role in this trend, including operational, thermodynamic, and kinetic factors.

First, the inlet temperature increased with the flow rate from a value of 62 °C (at 5 NL/min) to 103 °C (at 15 NL/min) because of the enhanced heat exchange between the pre-heating cartridge and the gas flow with increasing flow rate. Thus, the adiabatic equilibrium temperature also increased; the single values calculated for the various experiments are reported as short dotted bars at the right-hand side of Figure 2. Secondly, as better shown in Figure 3a, the measured outlet temperature increased more markedly than the adiabatic temperature; thus, the difference between the outlet adiabatic equilibrium temperature and the outlet measured temperature decreased with the increase of the flow rate.

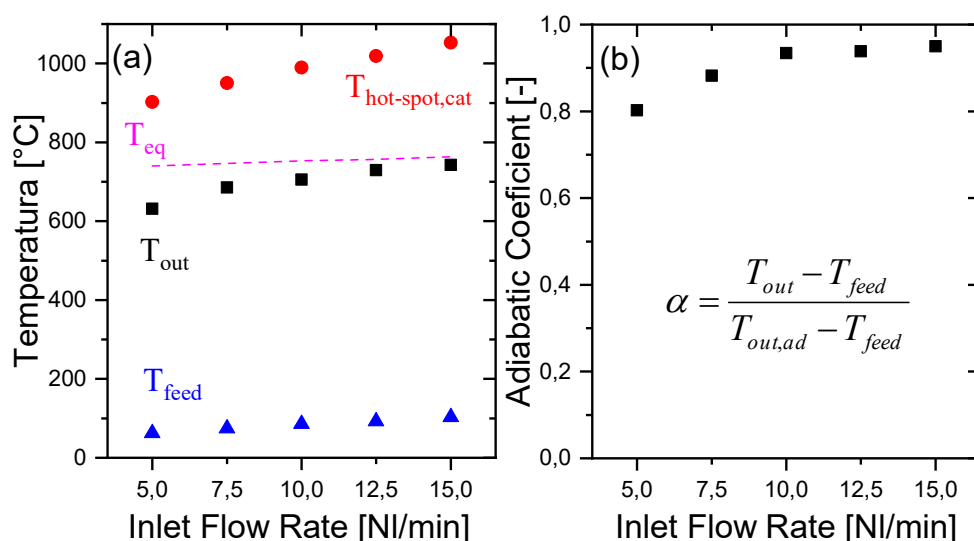


**Figure 3.** Effect of flow rate. Flow rate: (a) adiabaticity coefficient and (b) temperatures. Feed composition: iC8 = 3%, air with C/O = 0.9 and N<sub>2</sub> complement.

In other words, at increasing load, the reactor better approached the adiabatic behavior. This effect can be quantified through the definition of an adiabaticity coefficient, expressing the ratio between the measured temperature rise across the CPO reactor and ideal temperature rise for the fully adiabatic reactor, as follows:

$$\alpha = \frac{T_{out} - T_{feed}}{T_{out,ad} - T_{feed}} \quad (1)$$

As shown in panel (b) of Figure 3, the adiabaticity coefficient increased significantly with the flow rate, passing from a value of 80% in the case of 5 NL/min, to 93% in the case of 10 NL/min, and finally to 95% in the case of 15 NL/min. This trend reveals the impact of heat dispersions on the thermal balance of the reactor or, in other words, the relative impact of heat dispersion over heat load. The data clearly show that although heat dispersions expectedly grew on absolute basis due to the progressive increase of the reactor temperature, the ratio between heat dispersion and the inlet enthalpy flux entering the reactor decreased. The criticality of obtaining a full adiabatic behavior at the lab scale is well known, and this is especially true when dealing with miniaturized systems, given the high surface-to-volume ratio; thus, the experiments were extremely important to verify the sensitivity of the system to a key parameter as input flow. It was concluded that at total flows above 10 NL/min, the CPO reactor can be treated as fully adiabatic.

Lastly, it is observed that another important phenomenon was the increase and enlargement of the hot spot region at increasing flow rate (as shown in Figure 2 and highlighted in Figure 3, panel (a)), which cannot be explained by the above-mentioned factors. A modelling analysis was thus performed

to understand more deeply the kinetic effects involved in the temperature profile, and its dependence on flow rate.

## 2.2. Modeling Analysis

To gain insight into the correlation between inlet flow rate and hot spot temperatures, the reactor was simulated, assuming a perfect adiabatic behavior. The predicted gas-phase and solid phase temperature profiles are reported in Figure 4.

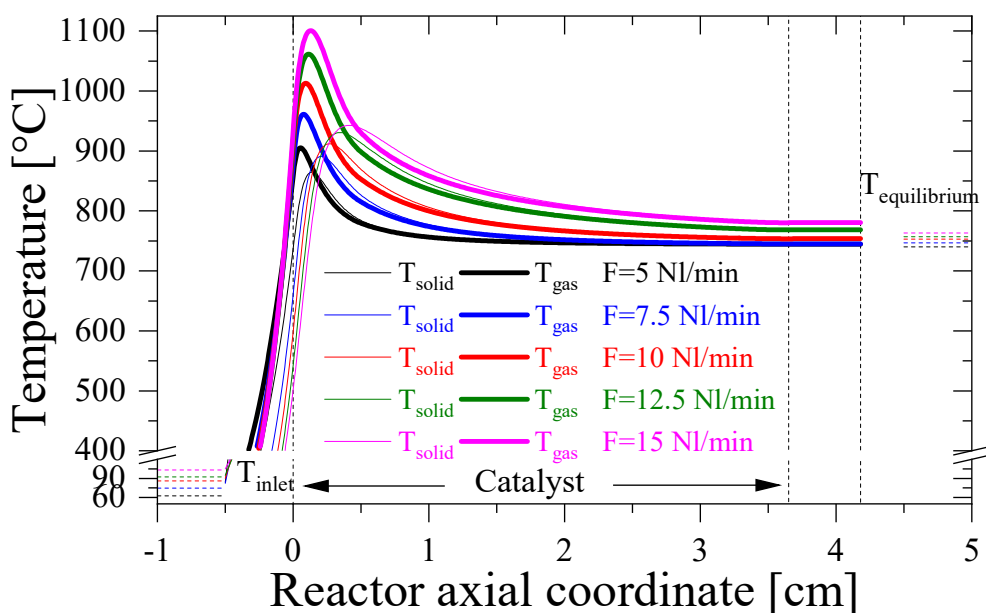


**Figure 4.** Simulated temperature profiles varying the inlet flow rate. Feed composition: iC8 = 3%, air with C/O = 0.9 and N<sub>2</sub> complement. Very good agreement with the experimental results was obtained, since the calculations showed a progressive increase of the whole temperature profiles and an especially important increase of temperatures in the hot spot at the monolith entrance.

Notably, a progressive enlargement of the hot spot is predicted; in fact, the decline of the temperature downstream of the maximum becomes more gradual at increasing flow, such that at any flow rate, the consumption of O<sub>2</sub> is more rapid than the consumption of i-C8 and the formation of CO and H<sub>2</sub> starting from the very entrance of the monolith. Thus, the heat release occurs across a shorter distance than heat consumption, which originates from the hot spot at the entrance.

The simulated concentration profiles are reported in Figure 5.

Panels (a) and (b) present a progressive extension of the iso-C<sub>8</sub>H<sub>18</sub> and O<sub>2</sub> consumption zones with inlet flow increase. In fact, a higher flow rate corresponds to a higher velocity of the gas phase inside the reactor; thus, there is an expected delay of consumption of the reactants. In particular, the O<sub>2</sub>—consumption length (Figure 5b) grows from 0.25 cm (5 NL/min) to 0.75 cm (15 NL/min). This region is the so-called oxy-reforming zone, where the hot spots develop as the result of the balance between exothermic reactions responsible for O<sub>2</sub> consumption (mainly H<sub>2</sub> oxidation) and endothermic reactions responsible for the fuel consumption (iC8 steam reforming to CO and H<sub>2</sub>) [31].

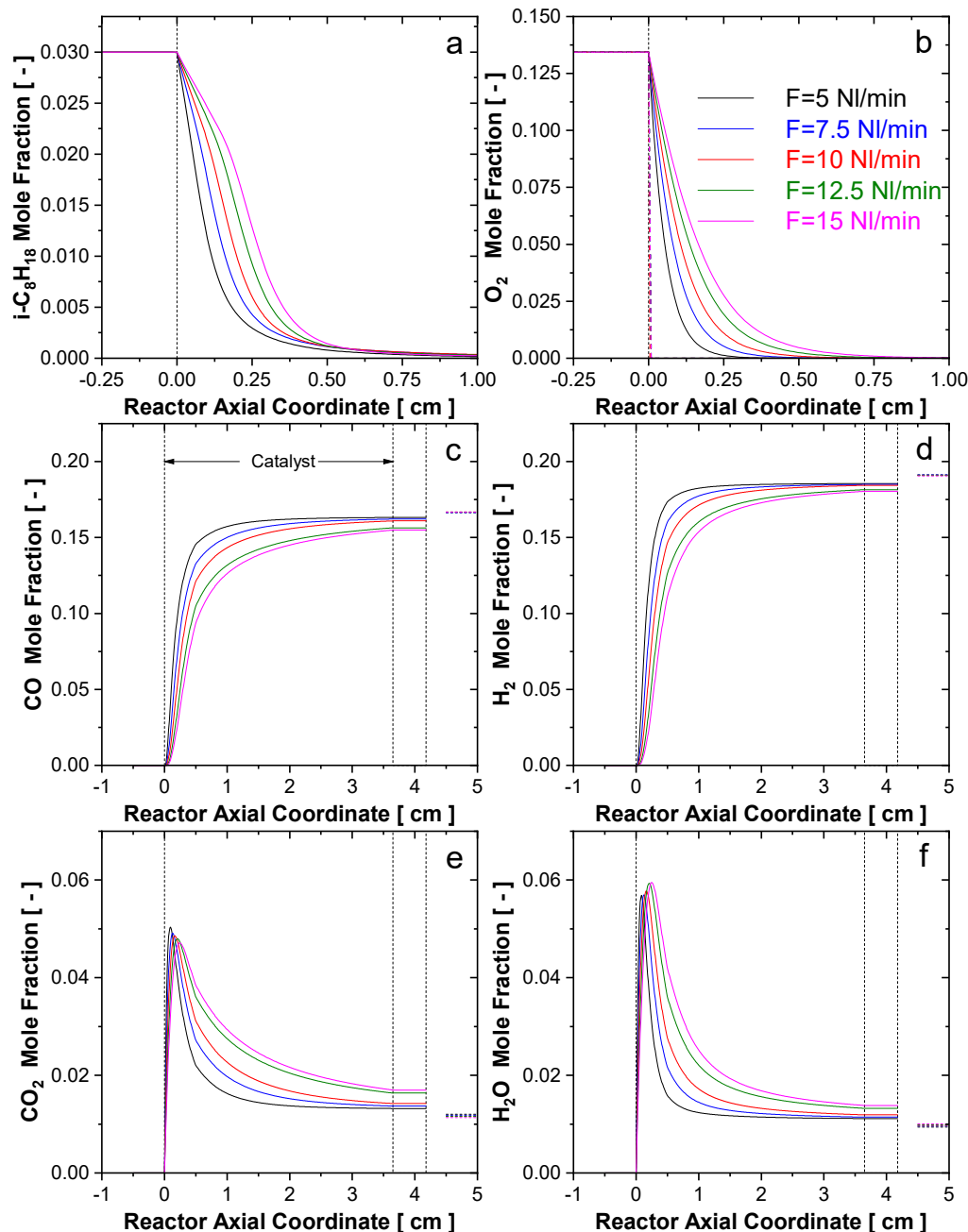


**Figure 5.** Simulated concentration profiles obtained varying the inlet flow. Feed composition:  $i\text{C}8 = 3\%$ , air with  $\text{C}/\text{O} = 0.9$  and  $\text{N}_2$  complement.

However, the balance between exothermic and endothermic reactions can change. This is more clearly shown in Figure 6, where the conversion profiles of the reactants are plotted in the various flow conditions; taking the coordinate 0.25 cm as a reference, here the oxygen conversion moves from 98% at 5 NL/min to 78% at 15 NL/min. On the other hand, iso-octane conversion moves from 88% of 5 NL/min to 53% of 15 NL/min. Thus, the exothermic contribution increases over the endothermic one and temperatures grow consequently. A change of selectivity is also produced, leading to an increased concentration of  $\text{H}_2\text{O}$  and  $\text{CO}_2$  a decreased concentration of CO and  $\text{H}_2$ .

Such an unbalancing of exothermic and endothermic contributions is fuel-specific, being related to the slow diffusivity of  $i\text{-C}8$ , which enhances the consecutive nature of the surface process [2], and to its high gas phase reactivity, which results in the onset of homogeneous reactions upon an ignition delay. The onset of gas phase reactions is progressively shifted downstream on increasing the flow

rate, as evidenced by the change of slope of iC8 conversion curves in Figure 6. In addition to this fuel-specific effect, there is also a general trend associated with the increase of gas velocity in CPO processes: at increasing importance of convection, conduction is less effective in smoothing the surface hot spot [32].

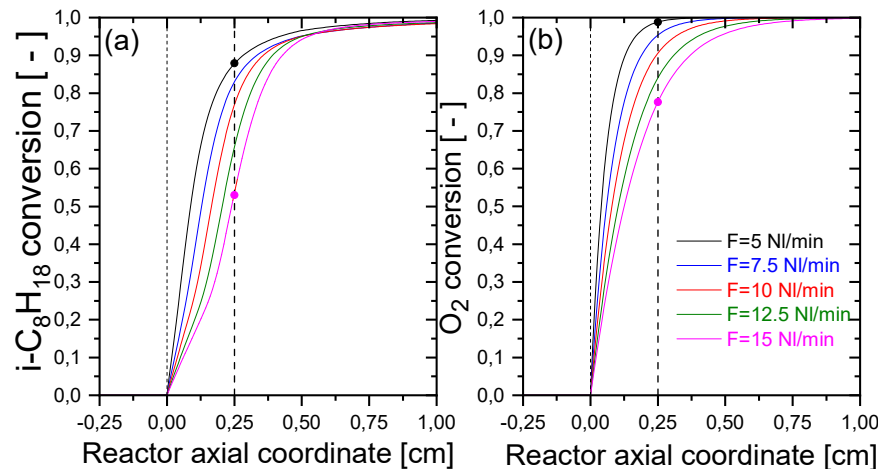


**Figure 6.** Effect of flow rate: (a) i-C<sub>8</sub>H<sub>18</sub> conversion and (b) O<sub>2</sub> conversion. Feed composition: iC8 = 3%, air with C/O = 0.9 and N<sub>2</sub> complement.

### 2.3. Catalyst Stability

The effect on the catalyst stability of performing iC8 experiments at increasing flow rate, and thus the effect of exposing the catalyst to progressively temperature increase, was verified by systematically repeating methane CPO tests; these were carried out on the fresh catalyst and after every iso-octane CPO test.

The reactor integral performance was measured, and the results are reported in Table 1, in terms of reactant conversion and product selectivity. Negligible differences were observed between the experiment on fresh catalyst and the following tests, and a close approach to thermodynamic equilibrium was found.

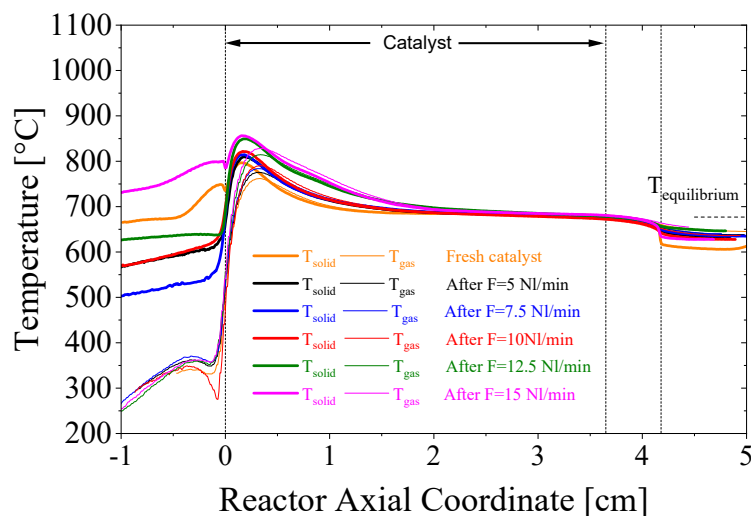
**Table 1.** Methane CPO: reactants conversion and products selectivity.

Table	$\chi\text{CH}_4$	$\chi\text{O}_2$	$\sigma\text{H}_2$	$\sigma\text{CO}$	$\sigma\text{CO}_2$	$\sigma\text{H}_2\text{O}$
	[·]	[·]	[·]	[·]	[·]	[·]
equilibrium	0.86	1.00	0.92	0.86	0.14	0.08
fresh catalyst	0.84	1.00	0.90	0.84	0.16	0.10
after 5 NL/min	0.84	1.00	0.90	0.85	0.15	0.10
after 7.5 NL/min	0.84	1.00	0.90	0.85	0.15	0.10
after 10 NL/min	0.84	1.00	0.90	0.85	0.15	0.10
after 12.5 NL/min	0.84	1.00	0.90	0.85	0.15	0.10
after 15 NL/min	0.84	1.00	0.90	0.84	0.16	0.10

More sensitive data were, however, obtained from the axially resolved temperature measurements shown in Figure 7.

The outlet temperature remained aligned with the adiabatic equilibrium, but changes of the temperature profiles were observed in the entering zone. In fact, the fresh catalyst showed a hot spot of temperature of about 780 °C and flattening of the solid and gas temperature profiles (which indicates where the system approaches the thermodynamic equilibrium) at about 1.5 cm from the entrance. Test after test, the maxima measured by the thermocouple and the pyrometer, as well as the axial extension of the hot spot, increased. After the iC8 experiment at 15 NL/min, the hot spot temperature

measured by the optical fiber amounted to 856 °C, while the flattening of the solid and gas-phase temperatures was observed in correspondence with the coordinate of 2.5 cm.



**Figure 7.** Effect of flow rate variation on the catalyst stability.  $\text{CH}_4 = 27.3\%$ , air with C/O = 0.9, and  $T_{in} = 25\text{ }^{\circ}\text{C}$ ,  $F = 10\text{ NL/min}$ . ( $T_{solid}$  measured with an optical fiber and  $T_{gas}$  measured with a thermocouple).

This is the clear evidence of a progressive deactivation of the catalyst, likely due to sintering of Rh clusters after exposure to temperature exceeding 900 °C in the iC8 experiments. The phenomenology of deactivation has been discussed in previous works from this and other research groups [14,32,33]. Since  $\text{O}_2$  consumption in the oxidation reactions is fully mass transfer controlled, while  $\text{CH}_4$  consumption via steam reforming is more chemically controlled, a loss of surface sites will preferentially affect the steam reforming reaction, with a consequent loss of the heat consumption rate and thus an increase of temperatures in the oxy-reforming zone.

Despite the deactivation probed by the temperature measurements, the evidence that equilibrium conversion and syngas yield were still reached in every  $\text{CH}_4$  CPO test confirms that the monolith was sufficiently oversized for keeping a stable methane CPO application.

Taking into consideration all the results obtained, methane CPO tests confirm that, when feeding a logistic fuel such as iso-octane, a flow rate of 10 NL/min is a relatively safe condition that is able to preserve catalyst stability and avoid an important deactivation via sintering.

### 3. Materials and Methods

#### 3.1. Catalyst Synthesis, Structural and Morphological Characterizations

The catalyst evaluated in this work is a sample of 400/7 cordierite honeycomb monolith, coated with a 2 wt% Rh/α-Al<sub>2</sub>O<sub>3</sub> active phase. The Rh/α-Al<sub>2</sub>O<sub>3</sub> catalytic powder was synthesized by incipient wetness impregnation of α-Al<sub>2</sub>O<sub>3</sub> with Rh(NO<sub>3</sub>)<sub>3</sub> solution, followed by drying at 120 °C overnight. Surface area and pore size volume of the catalyst powders, respectively, 5 m<sup>2</sup>/g and 0.21 mL/g, were determined by N<sub>2</sub> adsorption–desorption at 77 K with the BET method using a Micromeritics TriStar 3000 instrument. Rhodium content, 1.71% w/w, was determined by ICP-MS using a XSeries instrument.

Rh dispersion on the catalyst powders was estimated by hydrogen pulse chemisorption using a TPD/R/O 1100 Thermo Fischer Instrument. A pre-treatment was performed consisting of an initial reduction with a 5% H<sub>2</sub>/Ar flow (50 Ncm<sup>3</sup>/min) from room temperature up to 500 °C (heating rate 7 °C/min). After 1h at 500 °C, the sample was cooled down to 40 °C in pure Argon. The chemisorption was performed with 20–30 pulses (0.86 Ncm<sup>3</sup>) of the same diluted H<sub>2</sub> mixture. Ageing experiments under reaction atmosphere were performed in order to evaluate the catalyst stability using mild

(4% CH<sub>4</sub>, C/O = 0.9, N<sub>2</sub> to balance) and severe (27% CH<sub>4</sub> in air with C/O = 0.9) conditions, ramping the temperature from R.T to 850 °C (heating rate 10 °C/min, 850 °C hold for 4h) at GHSV = 80,000 NL/kg/h. The results of chemisorption on the fresh and aged catalysts are presented in Table 2, showing a progressive decrease of Rh dispersion from 69% for the as prepared catalyst to 7% under severe ageing conditions, which resemble those achieved in the adiabatic reactor.

**Table 2.** Catalyst morphological characteristics.

Catalyst	Rh Load			Rh Dispersion (%)
	% w/w	Fresh	Aged (4% CH <sub>4</sub> )	Aged (27% CH <sub>4</sub> )
Rh/α-Al <sub>2</sub> O <sub>3</sub>	1.71	69	23	7

After drying, the catalyst powders were suspended with water and nitric acid before undergoing a 24h-long ball milling. The coating proceeded through the dip-coating technique. Further details on synthesis methodology can be found elsewhere [34].

Aiming to verify the presence of heat losses along the reactor, the monolith was partly uncoated, in the rear part, forming a continuous back heat shield (CBHS), being completely coated at the entrance and avoiding a continuous front heat shield, thus reducing the hot spot temperature.

Table 3 reports the characteristics of the catalyst used in this work.

**Table 3.** Catalyst specifications.

Catalyst	L <sub>cat</sub> [cm]	LCBHS [cm]	m <sub>cat</sub> [g]	t <sub>cat</sub> [μm]	Void Fraction [-]
Rh/α-Al <sub>2</sub> O <sub>3</sub>	3.65	0.53	0.63	9.43	0.714

L<sub>cat</sub> = catalyst length; LCBHS = continuous back heat shield length; m<sub>cat</sub> = catalyst deposited mass; t<sub>cat</sub> = catalyst thickness.

The catalysts were inserted in a quartz pipe between a FeCrAlloy 15 ppi foam and an inert cordierite monolith inserted in such a way to guarantee downstream position to the back-heat shield.

### 3.2. Experimental Setup

A capillary (ID 320 μm), carefully allocated in a central channel of the catalyst, was capable to slide along the axial coordinate, as the reactor is equipped with spatially resolved sampling apparatus. Two different types of capillaries are employed in alternance: a (ID = 200 μm, OD = 350 μm), opened at its tip, allowing collecting gas samples and a second capillary (OD = 500 μm), closed at its tip, used to host the 250 μm K-Type thermocouple or a 45° ground optical fiber. Optical fiber and thermocouple are used to collect, respectively, the temperatures of the solid and gas phase. An Agilent MicroGC 3000A equipped with two columns (Plot U and a Molecular Sieve, Agilent, Santa Clara, CA, USA) was used to determine the gas phase concentration of different species. Plot U was operated at 60 °C, in order to get better resolution for light hydrocarbons (C1–C4) and then at 160 °C in order to get peaks of small tailing effect. N<sub>2</sub> was chosen as internal standard. As Plot U is not capable to separate N<sub>2</sub> from CH<sub>4</sub>, O<sub>2</sub>, H<sub>2</sub>, and CO, the Molecular Sieve was used as well.

The effect of the inlet flow rate on CPO of iC8 was conducted with a progressive increase of the total flow from 5 NL/min to 15 NL/min. The inlet concentration of the hydrocarbon was 3%, and the C/O ratio was kept constant and equal to 0.9. The goal of this campaign is to evaluate the adiabaticity of the reactor and the activity of the catalyst. The stability of the catalyst has been evaluated, by performing methane CPO tests on the fresh catalyst and after each iso-octane experiment.

### 3.3. Reactor Modelling

A mathematical 1D, dynamic, fixed bed, heterogeneous, single channel reactor model was used for the reactor design and for the analysis of experimental results. Its development was presented in previous works [16,34].

The model accounts for axial convection and diffusion, gas–solid transport term, solid conduction, and mass and energy balances for both solid and gas phase (Table 4).

**Table 4.** Model equations.

<b>Gas Phase</b>	
Mass Balance	$\frac{\partial \omega_i}{\partial t} = -\frac{G}{\rho_g \varepsilon} \frac{\partial \omega_i}{\partial z} - \frac{a_v}{\varepsilon} k_{mat,i} (\omega_i - \omega_{wall,i}) + \frac{\mathfrak{D}_{i,mix}}{\varepsilon} \frac{\partial^2 \omega_i}{\partial z^2} + MW_i \sum_{j=1}^{NR_s} v_{i,j} r_j^{homo}$
Enthalpy Balance	$\frac{\partial T_g}{\partial t} = -\frac{G}{\rho_g \varepsilon} \frac{\partial T_g}{\partial z} - \frac{a_v h(T_g - T_s)}{\varepsilon \rho_g \hat{c}_{p,g}} - \sum_{j=1}^{NR_s} \Delta H_{r,j} r_j^{homo}$
<b>Solid Phase</b>	
Mass Balance	$0 = a_v \rho_g k_{mat,i} (\omega_i - \omega_{wall,i}) + \frac{MW_i \rho_w \alpha}{\rho_s \hat{S}_{att}} \eta \sum_{j=1}^{NR_s} v_{i,j} r_j^{het}$
Enthalpy Balance	$\frac{\partial T_s}{\partial t} = \frac{a_v h(T_g - T_s)}{(1-\varepsilon) \rho_s \hat{c}_{p,s}} + \frac{\frac{\partial}{\partial z} (k_{ax}^{eff} \frac{\partial T_s}{\partial z})}{(1-\varepsilon) \rho_s \hat{c}_{p,s}} + \frac{\alpha}{(1-\varepsilon) \rho_s \hat{c}_{p,s} \hat{S}_{att}} \eta \sum_{j=1}^{NR_s} \Delta H_{r,j} r_j^{het}$
<b>Boundary Conditions</b>	
Reactor Inlet	$\omega_i _{z=0} = \omega_{i,feed}$
Reactor Outlet	$\frac{\partial \omega_i}{\partial z} _{z=L} = 0$
Initial Conditions	$\omega_i(z,0) = 0$
	$T_g _{z=0} = T_{feed}$
	$\frac{\partial T_s}{\partial z} _{z=0} = 0$
	$T_g(z,0) = T_{feed}$
	$T_s(z,0) = 650 \text{ } ^\circ\text{C}$

This model is an extension of a previous, already validated methane CPO model, now taking into consideration a catalytic kinetic scheme for i-C<sub>8</sub>H<sub>18</sub> conversion [30]. The gas phase kinetics are also included, as reported in [19].

The kinetic scheme is presented in Table 5.

**Table 5.** Heterogeneous reaction mechanism for iso-octane CPO [30,35,36].

Reaction Name and Chemical Equation	Rate Equation [mol/atm/g <sub>cat</sub> /s]	k <sub>i</sub> @873K [mol/atm/g <sub>cat</sub> /s]	E <sub>activation</sub> [kJ/mol]	Ref.
CH <sub>4</sub> oxidation CH <sub>4</sub> + 2 O <sub>2</sub> → CO <sub>2</sub> + 2 H <sub>2</sub> O	$r_{CH_4}^{OX} _{873K} = \frac{k_{CH_4}^{OX} p_{CH_4}}{1 + K_{H_2O}^{ads} p_{H_2O}} \sigma_{O_2}$	$1.030 \times 10^{-1}$	91.96	[33]
CH <sub>4</sub> steam reforming CH <sub>4</sub> + H <sub>2</sub> O → CO + 3 H <sub>2</sub>	$r_{CH_4}^{SR} _{873K} = \frac{k_{CH_4}^{SR} p_{CH_4}}{1 + K_{H_2O}^{ads} p_{H_2O} + K_{CO}^{ads} p_{CO}} \sigma_{H_2O} (1 - \eta_{CH_4}^{SR})$	$1.027 \times 10^{-1}$	91.80	[33]
CO methanation CO + 3 H <sub>2</sub> → CH <sub>4</sub> + H <sub>2</sub> O	$r_{CO}^{meth} _{873K} = \frac{k_{CO}^{meth} p_{H_2} \sigma_{CO}}{1 - \eta_{CO}^{meth}}$	$1.500 \times 10^{-3}$	30.00	[26]
Water Gas Shift CO + H <sub>2</sub> O → CO <sub>2</sub> + H <sub>2</sub>	$r_{WGS} _{873K} = \frac{k_{WGS} p_{H_2O} \sigma_{CO}}{1 - \eta_{WGS}}$	$6.831 \times 10^{-3}$	74.83	[33]
Reverse Water Gas Shift CO <sub>2</sub> + H <sub>2</sub> → CO + H <sub>2</sub> O	$r_{RWGS} _{873K} = \frac{k_{RWGS} p_{CO_2} \sigma_{H_2}}{1 - \eta_{RWGS}}$	$1.277 \times 10^{-2}$	62.37	[26]
H <sub>2</sub> oxidation H <sub>2</sub> + 1/2 O <sub>2</sub> → H <sub>2</sub> O	$r_{H_2}^{OX} _{873K} = k_{H_2}^{OX} p_{H_2} \sigma_{O_2}$	$2.666 \times 10^3$	61.65	[33]
CO oxidation CO + 1/2 O <sub>2</sub> → CO <sub>2</sub>	$r_{CO}^{OX} _{873K} = k_{CO}^{OX} p_{CO} \sigma_{O_2}$	$1.937 \times 10^1$	76.07	[33]
iso-C <sub>8</sub> H <sub>18</sub> total oxidation iso-C <sub>8</sub> H <sub>18</sub> + 25/2 O <sub>2</sub> → 8 CO <sub>2</sub> + 9 H <sub>2</sub> O	$r_{i-C_8H_{18}}^{OX} _{873K} = \frac{k_{i-C_8H_{18}}^{OX} p_{i-C_8H_{18}}}{1 + K_{H_2O}^{ads} p_{H_2O}} \sigma_{O_2}$	$4.600 \times 10^{-1}$	80.00	[34]

Table 5. Cont.

Reaction Name and Chemical Equation	Rate Equation [mol/atm/g <sub>cat</sub> /s]	k <sub>i</sub> @873K [mol/atm/g <sub>cat</sub> /s]	E <sub>activation</sub> [kJ/mol]	Ref.
iso-C <sub>8</sub> H <sub>18</sub> steam reforming iso-C <sub>8</sub> H <sub>18</sub> + 8 H <sub>2</sub> O → 8 CO + 17 H <sub>2</sub>	$r_{i-C_8H_{18}}^{SR} \Big _{873K} = \frac{k_{i-C_8H_{18}}^{SR} p_{i-C_8H_{18}}}{1 + K_{i-C_8H_{18}}^{\text{poison}} \frac{p_{i-C_8H_{18}}}{p_{H_2O}}} \sigma_{H_2O} (1 - \eta_{i-C_8H_{18}}^{SR})$	$7.500 \times 10^{-2}$	69.00	[34]
	$r_j^{\text{chemical reaction}} = r_j^{\text{chemical reaction}} \Big _{873K} \exp \left[ -\frac{E_{att, j}}{R} \left( \frac{1}{T} - \frac{1}{873} \right) \right]$			
Adsorption	K <sub>i</sub> <sup>0,ads</sup> @873K [1/atm]	ΔH <sub>adsorption</sub> [kJ/mol]	Ref.	
O <sub>2</sub>	$5.461 \times 10^0$	-72.83	[33]	
CO	$2.114 \times 10^2$	-37.15	[33]	
H <sub>2</sub> O	$8.974 \times 10^0$	-57.48	[33]	
Poisoning term	K <sub>i</sub> <sup>0, poisoning</sup> @873K [-]	ΔH <sub>adsorption</sub> [kJ/mol]	Ref.	
i-C <sub>8</sub> H <sub>18</sub>	$6.000 \times 10^0$	-26.00	[34]	
n-C <sub>8</sub> H <sub>18</sub>	$6.000 \times 10^0$	-26.00	[34]	
	$r_j = K_j^0 \exp \left[ -\frac{E_{att, r_j}}{R} \left( \frac{1}{T} - \frac{1}{873} \right) \right]$			

#### 4. Conclusions

Rhodium supported catalysts, operated in adiabatic reactors, are effective in the small-scale production of synthesis gas from liquid fuels. These features make this process attractive for the development of a compact reformer. Rhodium-based catalysts are able to efficiently reform iso-octane into synthesis gas.

Experiments and model simulations confirm the indirect reaction mechanism, which is responsible for the presence of an oxy-reforming zone in the first part of the catalyst and a reforming zone further downstream.

It has been observed that the increase of the inlet flow rate promotes the adiabaticity of the reactor, but it leads to a higher catalyst hot spot temperature, due to the higher inlet enthalpic flux. The catalyst stability has been evaluated by performing a methane CPO after each octane test. The optimal inlet flow rate has been set to 10 NL/min, the setting that guarantees the best compromise between the adiabaticity of the reactor and the stability of the catalyst.

**Author Contributions:** The research was completed through the cooperation of all authors. All authors were responsible for the study of concept, data acquisition and interpretation. G.G. and A.B. were responsible for the project's conceiving and design, being also responsible for drafting and revising the manuscript.

**Funding:** This research was funded by MIUR—Ministero dell’Istruzione, dell’Università e della Ricerca (Italy) within the PRIN—2015 program, HERCULES project; and by MISE—Ministero dello Sviluppo Economico (Italy) within the Industria 2015 program, MICROGEN 30 project.

**Conflicts of Interest:** The authors declare no conflict of interest.

#### References

- U.S. Energy Information Administration. *International Energy Outlook 2017*; U.S. Energy Information Administration: Washington, DC, USA, 2017.
- Carrera, A.; Beretta, A.; Groppi, G. Catalytic Partial Oxidation of Iso-Octane over Rh/α-Al<sub>2</sub>O<sub>3</sub> in an Adiabatic Reactor: An Experimental and Modeling Study. *Ind. Eng. Chem. Res.* **2017**, *56*, 4911–4919. [[CrossRef](#)]
- Yvonne, R.; Simon, L.; Johannes Pfister, C.D. *Fuel Cells and Hydrogen for Green Energy in European Cities and Regions. A Study for the Fuel Cells and Hydrogen Joint Undertaking*; Sederanger: Frankfurt, Germany, 2018.
- Farrauto, R.J.; Liu, Y.; Ruettinger, W.; Ilinich, O.; Shore, L.; Giroux, T. Precious Metal Catalysts Supported on Ceramic and Metal Monolithic Structures for the Hydrogen Economy. *Catal. Rev.* **2007**, *49*, 141–196. [[CrossRef](#)]

5. Heck, R.M.; Gulati, S.; Farrauto, R.J. The Application of Monoliths for Gas Phase Catalytic Reactions. *Chem. Eng. J.* **2001**, *82*, 149–156. [[CrossRef](#)]
6. Farrauto, R.; Hwang, S.; Shore, L.; Ruettinger, W.; Lampert, J.; Giroux, T.; Liu, Y.; Ilinich, O. New Material Needs for Hydrocarbon Fuel Processing: Generating Hydrogen for the PEM Fuel Cell. *Annu. Rev. Mater. Res.* **2003**, *33*, 1–27. [[CrossRef](#)]
7. Groppi, G.; Tronconi, E. Honeycomb Supports with High Thermal Conductivity for Gas/Solid Chemical Processes. *Catal. Today* **2005**, *105*, 297–304. [[CrossRef](#)]
8. Specchia, S. Fuel Processing Activities at European Level: A Panoramic Overview. *Int. J. Hydrol. Energy* **2014**, *39*, 17953–17968. [[CrossRef](#)]
9. Kraaij, G.J.; Specchia, S.; Bolito, G.; Mutri, L.; Wails, D. Biodiesel Fuel Processor for APU Applications. *Int. J. Hydrol. Energy* **2009**, *34*, 4495–4499. [[CrossRef](#)]
10. Specchia, S.; Tillemans, F.W.A.; van den Oosterkamp, P.F.; Saracco, G. Conceptual Design and Selection of a Biodiesel Fuel Processor for a Vehicle Fuel Cell Auxiliary Power Unit. *J. Power Sources* **2005**, *145*, 683–690. [[CrossRef](#)]
11. Kolb, G.; Baier, T.; Schürer, J.; Tiemann, D.; Ziogas, A.; Specchia, S.; Galletti, C.; Germani, G.; Schuurman, Y. A Micro-Structured 5 kW Complete Fuel Processor for Iso-Octane as Hydrogen Supply System for Mobile Auxiliary Power Units Part II—Development of Water–Gas Shift and Preferential Oxidation Catalysts Reactors and Assembly of the Fuel Processor. *Chem. Eng. J.* **2008**, *138*, 474–489. [[CrossRef](#)]
12. Hou, Z.; Chen, P.; Fang, H.; Zheng, X.; Yashima, T. Production of Synthesis Gas via Methane Reforming with CO<sub>2</sub> on Noble Metals and Small Amount of Noble-(Rh-) Promoted Ni Catalysts. *Int. J. Hydrol. Energy* **2006**, *31*, 555–561. [[CrossRef](#)]
13. le Saché, E.; Santos, J.; Smith, T.J.; Centeno, M.A.; Arellano-Garcia, H.; Odriozola, J.A.; Reina, T.R. Multicomponent Ni-CeO<sub>2</sub> Nanocatalysts for Syngas Production from CO<sub>2</sub>/CH<sub>4</sub> Mixtures. *J. CO<sub>2</sub> Util.* **2018**, *25*, 68–78.
14. Tavazzi, I.; Beretta, A.; Groppi, G.; Maestri, M.; Tronconi, E.; Forzatti, P. Experimental and Modeling Analysis of the Effect of Catalyst Aging on the Performance of a Short Contact Time Adiabatic CH<sub>4</sub>-CPO Reactor. *Catal. Today* **2007**, *129*, 372–379. [[CrossRef](#)]
15. Fichtner, M.; Mayer, J.; Wolf, D.; Schubert, K. Microstructured Rhodium Catalysts for the Partial Oxidation of Methane to Syngas under Pressure. *Ind. Eng. Chem. Res.* **2001**, *40*, 3475–3483. [[CrossRef](#)]
16. Maestri, M.; Beretta, A.; Groppi, G.; Tronconi, E.; Forzatti, P. Comparison among Structured and Packed-Bed Reactors for the Catalytic Partial Oxidation of CH<sub>4</sub> at Short Contact Times. *Catal. Today* **2005**, *105*, 709–717. [[CrossRef](#)]
17. Qi, A.; Wang, S.; Ni, C.; Wu, D. Autothermal Reforming of Gasoline on Rh-Based Monolithic Catalysts. *Int. J. Hydrol. Energy* **2007**, *32*, 981–991. [[CrossRef](#)]
18. Costa, D.S.; Gomes, R.S.; Rodella, C.B.; da Silva, R.B.; Fréty, R.; Teixeira Neto, É.; Brandão, S.T. Study of Nickel, Lanthanum and Niobium-Based Catalysts Applied in the Partial Oxidation of Methane. *Catal. Today* **2018**. [[CrossRef](#)]
19. Carrera, A.; Pelucchi, M.; Stagni, A.; Beretta, A.; Groppi, G. Catalytic Partial Oxidation of n-Octane and Iso-Octane: Experimental and Modeling Results. *Int. J. Hydrol. Energy* **2017**, *42*, 24675–24688. [[CrossRef](#)]
20. Nogare, D.D.; Degenstein, N.J.; Horn, R.; Canu, P.; Schmidt, L.D. Modeling Spatially Resolved Data of Methane Catalytic Partial Oxidation on Rh Foam Catalyst at Different Inlet Compositions and Flowrates. *J. Catal.* **2011**, *277*, 134–148. [[CrossRef](#)]
21. Panuccio, G.J.; Williams, K.A.; Schmidt, L.D. Contributions of Heterogeneous and Homogeneous Chemistry in the Catalytic Partial Oxidation of Octane Isomers and Mixtures on Rhodium Coated Foams. *Chem. Eng. Sci.* **2006**, *61*, 4207–4219. [[CrossRef](#)]
22. Wanat, E.C.; Venkataraman, K.; Schmidt, L.D. Steam Reforming and Water–Gas Shift of Ethanol on Rh and Rh–Ce Catalysts in a Catalytic Wall Reactor. *Appl. Catal. A Gen.* **2004**, *276*, 155–162. [[CrossRef](#)]
23. Degenstein, N.; Subramanian, R.; Schmidt, L. Partial Oxidation of n-Hexadecane at Short Contact Times: Catalyst and Washcoat Loading and Catalyst Morphology. *Appl. Catal. A Gen.* **2006**, *305*, 146–159. [[CrossRef](#)]
24. Donazzi, A.; Maestri, M.; Michael, B.C.; Beretta, A.; Forzatti, P.; Groppi, G.; Tronconi, E.; Schmidt, L.D.; Vlachos, D.G. Microkinetic Modeling of Spatially Resolved Autothermal CH<sub>4</sub> Catalytic Partial Oxidation Experiments over Rh-Coated Foams. *J. Catal.* **2010**, *275*, 270–279. [[CrossRef](#)]

25. Maestri, M.; Beretta, A.; Faravelli, T.; Groppi, G.; Tronconi, E.; Vlachos, D.G. Two-Dimensional Detailed Modeling of Fuel-Rich H<sub>2</sub> Combustion over Rh/Al<sub>2</sub>O<sub>3</sub> Catalyst. *Chem. Eng. Sci.* **2008**, *63*, 2657–2669. [CrossRef]
26. Batista da Silva, R.; Brandão, S.T.; Lucotti, A.; Tommasini, M.S.; Castiglioni, C.; Groppi, G.; Beretta, A. Chemical Pathways in the Partial Oxidation and Steam Reforming of Acetic Acid over a Rh-Al<sub>2</sub>O<sub>3</sub> catalyst. *Catal. Today* **2017**, *289*, 162–172. [CrossRef]
27. Donazzi, A.; Livio, D.; Beretta, A.; Groppi, G.; Forzatti, P. Surface Temperature Profiles in CH<sub>4</sub> CPO over Honeycomb Supported Rh Catalyst Probed with in Situ Optical Pyrometer. *Appl. Catal. A Gen.* **2011**, *402*, 41–49. [CrossRef]
28. Beretta, A.; Donazzi, A.; Groppi, G.; Maestri, M.; Tronconi, E.; Forzatti, P. Gaining Insight into the Kinetics of Partial Oxidation of Light Hydrocarbons on Rh, through a Multiscale Methodology Based on Advanced Experimental and Modeling Techniques. *Catalysis* **2013**, *25*, 1–49.
29. Iaquaniello, G.; Antonetti, E.; Cucchiella, B.; Palo, E.; Salladini, A.; Guarinoni, A.; Lainati, A.; Basini, L. Natural Gas Catalytic Partial Oxidation: A Way to Syngas and Bulk Chemicals Production. In *Natural Gas—Extraction to End Use*; InTech: London, UK, 2012.
30. Pagani, D.; Batista, R.; Silva, D.; Moioli, E.; Donazzi, A.; Lucotti, A.; Tommasini, M.; Castiglioni, C.; Brandao, S.T.; Beretta, A.; et al. Annular Reactor Testing and Raman Surface Characterization of the CPO of i-Octane and n-Octane on Rh Based Catalyst. *Chem. Eng. J.* **2016**, *294*, 9–21. [CrossRef]
31. Beretta, A.; Groppi, G.; Carrera, A.; Donazzi, A. *Analysis of the Impact of Gas-Phase Chemistry in Adiabatic CPO Reactors by Axially Resolved Measurements*; Academic Press: Cambridge, MA, USA, 2017; pp. 161–201.
32. Beretta, A.; Groppi, G.; Lualdi, M.; Tavazzi, I.; Forzatti, P. Experimental and Modeling Analysis of Methane Partial Oxidation: Transient and Steady-State Behavior of Rh-Coated Honeycomb Monoliths. *Ind. Eng. Chem. Res.* **2009**, *48*, 3825–3836. [CrossRef]
33. Cimino, S.; Lisi, L.; Russo, G. Effect of Sulphur during the Catalytic Partial Oxidation of Ethane over Rh and Pt Honeycomb Catalysts. *Int. J. Hydrot. Energy* **2012**, *37*, 10680–10689. [CrossRef]
34. Livio, D.; Donazzi, A.; Beretta, A.; Groppi, G.; Forzatti, P. Experimental and Modeling Analysis of the Thermal Behavior of an Autothermal C<sub>3</sub>H<sub>8</sub> Catalytic Partial Oxidation Reformer. *Ind. Eng. Chem. Res.* **2012**, *51*, 7573–7583. [CrossRef]
35. Donazzi, A.; Beretta, A.; Groppi, G.; Forzatti, P. Catalytic Partial Oxidation of Methane over a 4% Rh/α-Al<sub>2</sub>O<sub>3</sub> catalyst. Part I: Kinetic Study in Annular Reactor. *J. Catal.* **2008**, *255*, 241–258. [CrossRef]
36. Pagani, D.; Livio, D.; Donazzi, A.; Beretta, A.; Groppi, G.; Maestri, M.; Tronconi, E. A Kinetic Analysis of the Partial Oxidation of C<sub>3</sub>H<sub>8</sub> over a 2% Rh/Al<sub>2</sub>O<sub>3</sub> Catalyst in Annular Microreactor. *Catal. Today* **2012**, *197*, 265–280. [CrossRef]



© 2019 by the authors. Licensee MDPI, Basel, Switzerland. This article is an open access article distributed under the terms and conditions of the Creative Commons Attribution (CC BY) license (<http://creativecommons.org/licenses/by/4.0/>).